crystals

MDPI

Article

Evaluation of the Structural Deviation of Cu/Cu_2O Nanocomposite Using the X-ray Diffraction Analysis Methods

Nguyen Hoang Lam [1], Ryan P. Smith [2], Nam Le [1], Chau Thi Thanh Thuy [1], Mohaseen S. Tamboli [3], Asiya M. Tamboli [3], Sultan Alshehri [4], Mohammed M. Ghoneim [5], Nguyen Tam Nguyen Truong [1,*] and Jae Hak Jung [1,*]

[1] School of Chemical Engineering, Yeungnam University, 280 Daehak-ro, Gyeongsan 38541, Korea; nhlam@tvu.edu.vn (N.H.L.); namleyu92@gmail.com (N.L.); chauthuy041091@gmail.com (C.T.T.T.)
[2] Department of Physics, California State University—East Bay, Hayward, CA 94542, USA; ryan.p.smith@csueastbay.edu
[3] Korea Institute of Energy Technology (KENTECH), 200 Hyeokshin-ro, Naju 58330, Korea; tamboli.mohseen@gmail.com (M.S.T.); asiyashaikh2020@gmail.com (A.M.T.)
[4] Department of Pharmaceutical Sciences, College of Pharmacy, AlMaarefa University, Riyadh 13713, Saudi Arabia; sshehri.c@mcst.edu.sa
[5] Department of Pharmacy Practice, College of Pharmacy, Almaarefa University, Ad Diriyah 13713, Saudi Arabia; mghoneim@mcst.edu.sa
* Correspondence: authors: tamnguyentn@ynu.ac.kr (N.T.N.T.); jhjung@ynu.ac.kr (J.H.J.); Tel.: +82-10-8699-2586 (J.H.J.)

Abstract: We successfully synthesized Cu/Cu_2O nanocomposites using the wet chemical synthesis method. All X-ray diffraction (XRD), Reference Intensity Ratio (RIR), and Rietveld refinement methods confirmed that the compounds Cu and Cu_2O are free of impurities. Scanning Electron Microscope (SEM) and Transmission electron microscopy (TEM) images show the morphology and interactions of Cu and Cu_2O in the structure. The formation mechanism is also explained by five stages: precursor, nucleation, growth, aging, and reduction. The changes in crystallization parameters under variations in reaction temperature (T_v) and stirring speed (S_v) were confirmed by agreement with the XRD database. The lattice constant in the crystal of nanocomposite increases with rising temperature in the reaction, leading to unit cell expansion, while increasing the stirring—rate leads to a random size distribution of the lattice parameter. Due to the imperfect growth of the crystal, the induced crystallite size was calculated using the Williamson-Hall model, and the precise lattice parameter values were calculated using the Nelson-Riley function.

Keywords: crystallization parameters; Cu/Cu_2O nanocomposite; Nelson-Riley function; Williamson-Hall; X-ray diffraction

Citation: Lam, N.H.; Smith, R.P.; Le, N.; Thuy, C.T.T.; Tamboli, M.S.; Tamboli, A.M.; Alshehri, S.; Ghoneim, M.M.; Truong, N.T.N.; Jung, J.H. Evaluation of the Structural Deviation of Cu/Cu_2O Nanocomposite Using the X-ray Diffraction Analysis Methods. *Crystals* **2022**, *12*, 566. https://doi.org/10.3390/cryst12040566

Academic Editor: Raghvendra Singh Yadav

Received: 23 March 2022
Accepted: 12 April 2022
Published: 18 April 2022

1. Introduction

Metal and semiconductor oxides are used in a variety of energy applications such as batteries, supercapacitors, solar cells, and photoelectrochemical cells. Among these, Cu_2O is attractive because of its optical characteristics, availability, abundance, and environmentally—friendly material, which has advantages such as low synthesis cost and ease of synthesis with various methods. For these reasons, it is widely used in sensors, photo—catalysts, and solar cells [1–3]. Nevertheless, Cu_2O still has drawbacks in optical applications because it has a higher e^-–h^+ recombination rate than other materials [3]. The incorporation of Cu and Cu_2O in hetero—junctions can enhance the photo—catalytic properties, and reaction efficiency. Moreover, it can reduce the e^-–h^+ recombination due to the photoelectron transferability of Cu in that composite material [4].

There are various methods reported for Cu_2O nanoparticles synthesis, such as the hydrothermal, the electro—deposition, the wet chemical method, and the thermal decomposition [5–7]. The wet chemical synthesis method is one of the methods that allows for

adjustment of the thermodynamic and kinetic parameters to control crystal parameters such as the shape, the size, and the composition of nanoparticles [8]. Hence, the electronic, the optical, and the reactive properties of their surfaces can also be changed. Studies of controlling crystalline parameters have demonstrated their influence on the extraordinary magnetic, electrical, optical, and mechanical properties of nanomaterials [9].

Crystals should grow perfectly in all directions. No crystal, however, is perfect due to its finite size [10]. Furthermore, under different conditions of synthesis, the crystallographic parameters of the nanoparticles will grow in different directions, thus making the crystal imperfect. Deviation in crystal growth under different conditions leads to broadening of diffraction peaks compared with those from a perfect, crystalline structure. Lattice strain and crystal size are the two main parameters used to evaluate the misalignment of crystal growth [10]. Therefore, a clear understanding of the crystal size changes under different synthesis conditions will assist in the control of crystal size and shape, and further, in the control of the application of structure—based nanoparticles. In this study, the XRD technique was used to analyze the change in crystallographic parameter. In addition, we evaluated the effects of stirring speed (S_v) and reaction temperature (T_v) on crystallographic parameters of Cu/Cu_2O nanocomposites.

Additionally, the Williamson-Hall method was used to recalculate the induced—lattice strain and induced—crystallite size; the Nelson-Riley function was applied to determine the precise lattice parameter; and the Rietveild refinement method was used to confirm the composition of our sample.

2. Materials and Methods

2.1. Materials and Methods

The chemicals were used in this study include copper sulfate pentahydrate ($CuSO_4 \cdot 5H_2O$, >99%), polyethylene glycol (PEG, MW 6000), L—ascorbic acid ($C_6H_8O_6$, >99%), and sodium hydroxide (NaOH, >97%). All chemicals were from the Sigma Aldrich Company and did not need to be purified when used during the experiment. Deionized (DI) water was used to dilute all chemicals.

2.2. Synthesis of Cu/Cu_2O PNCs

First, 50 mL precursor solution was obtained by mixing 1.0 mol/L $CuSO_4 \cdot 5H_2O$ and 1.0 g/L PEG (ratio 1:1). Second, 25 mL NaOH 1M was slowly added under the stirring condition for 15 min. Third, $C_6H_8O_6$ (0.25 mmol) was added drop—by—drop into the solution, stirring for 30 min. The synthesis was performed at S_v = 250 rpm and T_v = 40 °C (ST). From the synthesis conditions of the ST sample, the changes in T_v and S_v were applied to evaluate the change in the structure of Cu/Cu_2O PNCs. The included treatments were T1 = 60 °C, T2 = 80 °C, T3 = 100 °C, S1 = 350 rpm, S2 = 450 rpm, and S3 = 550 rpm. The experimental conditions and codes are given in Table 1.

Table 1. The conditional treatment of experiments.

Code	$CuSO_4 \cdot 5H_2O$ (M)	PEG (g/L)	NaOH (M)	$C_6H_8O_6$ (mmol)	$NaBH_4$ (M)	T_v (°C)	S_v (rpm)
ST	1.0	1.0	1.0	0.25	1.0	**40**	**250**
T1	1.0	1.0	1.0	0.25	1.0	**60**	250
T2	1.0	1.0	1.0	0.25	1.0	**80**	250
T3	1.0	1.0	1.0	0.25	1.0	**100**	250
S1	1.0	1.0	1.0	0.25	1.0	40	**350**
S2	1.0	1.0	1.0	0.25	1.0	40	**450**
S3	1.0	1.0	1.0	0.25	1.0	40	**550**

After the reaction, the powders were extracted by centrifuging the solutions at 5000 rpm for 20 min. The obtained powders were washed three times sequentially with DI water, ethanol, and then DI water again. Finally, the powders were dried on a hot plate at 95 °C until the mass remained constant.

2.3. Characterizations

The crystallite structure and chemical composition were measured as the powder XRD patterns obtained by the X-ray diffractometer under Cu—Kα radiation with λ = 1.54056 Å (Bruker D8 Focus, Model: PANalytical X' pert PRO, PANalytical, Almelo, The Netherlands). Samples (powder) were placed on a sample holder, and data were obtained using Cu Kα monochromatic radiation according to Bragg's Law convention. The data of the samples were also taken in the range of 10–80° angles using the step size of 0.02 (2θ) per second. The surface morphology of samples was analyzed by SEM (Model JEOL JSM—7400F, Yokogushi, Tokyo, Japan) and HRTEM (FEI Company, Hillsborough, OR, USA). The diagram structure of samples was plotted by VESTA software. The Rietveld refinement method was used to scan the composition of samples by MAUD software (version 2.61, University of Trento, Trentino, Italy), and phase quantification was investigated via the reference intensity ratio (RIR) method (Chung 1974) using the MATCH! software (version 3.13, Dr. Holger Putz, Crystal Impact, Bonn, Germany). In the MATCH! software, the content of each crystalline phase was calculated as Equation (1) [11]:

$$C_i(\%) = 100 \times \left(\frac{I_i}{k_i}\right) / \sum_{i=1}^{n}\left(\frac{I_i}{k_i}\right) \quad (1)$$

where C_i is the percentage content of ith phase, I_i is the integral intensity of ith phase, and k_i is the coefficient (RIR) for ith phase obtained from the PDF database.

3. Results

3.1. The Formation of Cu/Cu_2O Powder Nanocomposite

The formation of Cu/Cu_2O powder nanocomposite can be divided into five stages: precursor, nucleation, growth, aging, and reduction (Figure 1). First, the precursor chemical ($CuSO_4 \cdot 5H_2O$) was dissolved in DI water; it was dissociated to yield free Cu^{2+} ions in the solution. PEG was added as the capping agent to cover the ions; the capping agent increases the viscosity of the solution. As a result, the diffusion and movement of ions in the solution becomes more difficult; because there is a layer of sorbent (capping agent) on the surface of the particles, the capping agent prevents the agglomeration of the particles. Furthermore, with PEG encapsulation, it is difficult for the nanoparticles to self—align or gather together to form clusters. Accordingly, the resulting nanoparticles are smaller in size than the formed nanoparticles in solution without PEG [12]. Second, in the nucleation stage, the Cu^{2+} ions react with OH^- ions to form $Cu(OH)_2$ precipitation, the neighbor ions bond to each other and form the cluster. Over time, the increase in OH^- ions causes more $Cu(OH)_2$ precipitates to form. During the nucleation process, the solution changes from light blue to dark blue and finally to milky blue.

Third, the growth phase of NPs has two mechanisms: the reaction on the surface and the diffusion of monomers onto the surface [13]. The capping agent not only interacts with the precursor ions but also has an important role in the growth phase. After the formation of NPs, the capping agent protects the surface of those particles by creating a stable cover layer. Moreover, the physicochemical properties of NPs mostly depend on the interaction between the NP and capping agent due to its ability to modify the interaction between the external system and NPs [14]. Additionally, in the growth phase, clusters gather together so that the size of the NPs increases. Fourth, aging is commonly used in the synthesis of NPs, and macro or micro—changes in the solid phase can occur during this process [15]. At the end of the aging period, the size of the NPs does not grow any further. Finally, L—ascorbic acid is used as a reducing agent to reduce $Cu(OH)_2$ so that it precipitates to form Cu_2O

particles; this process is shown in Figure 2. At first, the L—ascorbic acid reduced the $Cu(OH)_2$ precipitates to Cu_2O, and then, water molecules and $C_6H_8O_7$ were released as the by—products of reaction. When excess acid is added, the surface of Cu_2O particles were continuously reduced, which formed Cu dots on the surface of NPs, and water molecules and $C_6H_6O_6$ were liberated. Because the reduction reactions occur unevenly on the entire surface of the nanoparticle, the Cu dots are scattered on the surface of the nanoparticle forming Cu/Cu_2O nanocomposite, but the surface is not completely reduced to form the core–shell structure. The high—resolution TEM technique was used to confirm this explanation (Figure 3b).

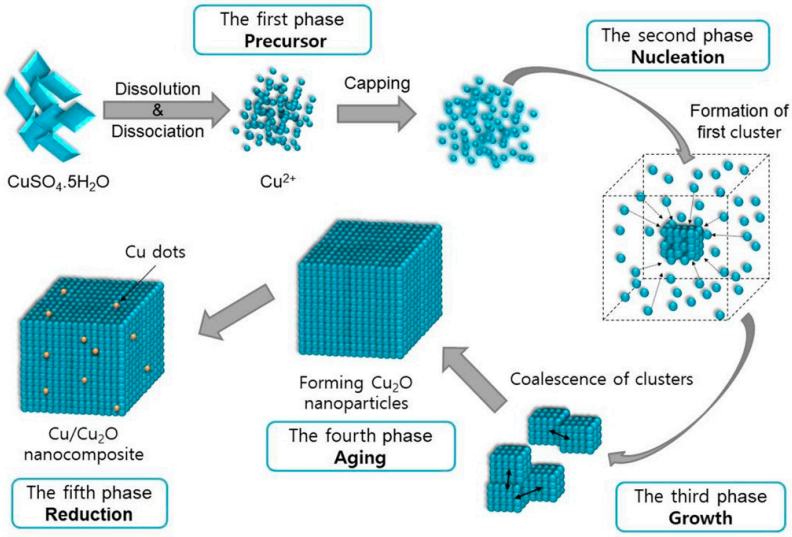

Figure 1. The diagram of the formation process of Cu/Cu_2O nanocomposite. This process was applied for all samples listed in Table 1 with different T_v and S_v.

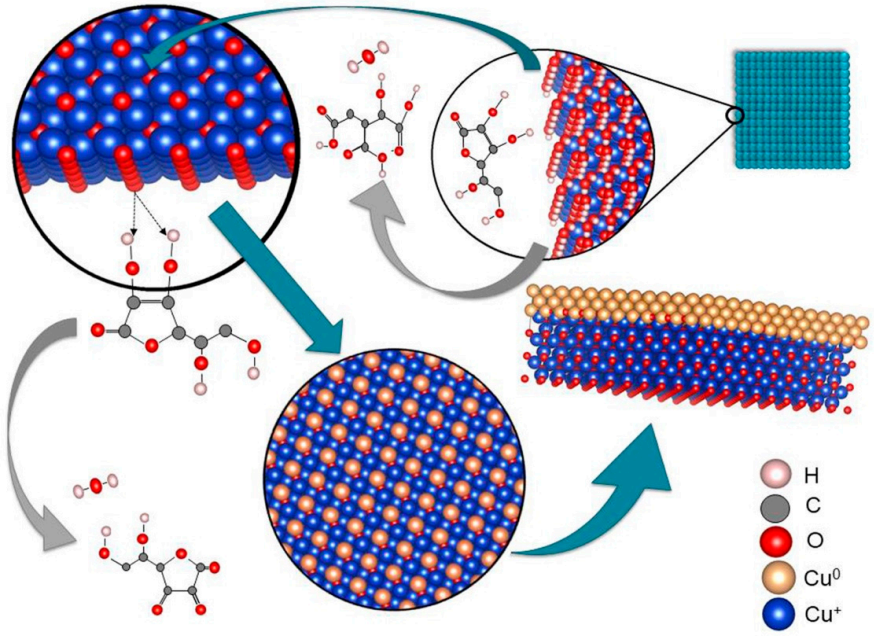

Figure 2. Reaction of reducing Cu_2O to Cu dost. This figure describes the reaction in the fifth phase of the synthesis process. The interaction between L—ascorbic acid and Cu_2O on the surface layer of the nanoparticle forms Cu dots on the surface. Products released from this reaction include water molecules and $C_6H_6O_6$. Since the reaction only occurs on the surface, only the outer Cu_2O layer is reduced to form Cu dots.

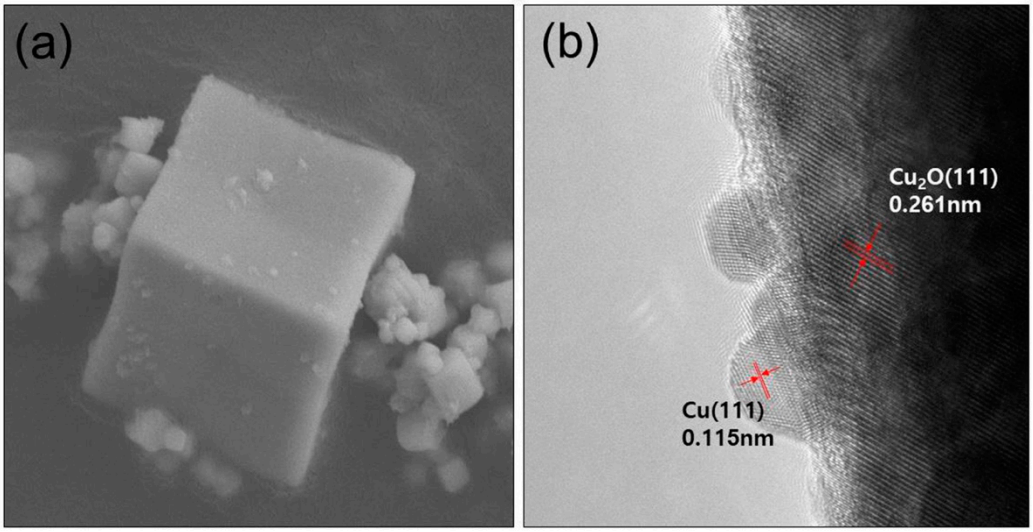

Figure 3. (**a**) SEM image and (**b**) HRTEM image of Cu/Cu_2O nanocomposite. This figure supports the previous figures. It shows the appearance of Cu dots and the surface of Cu_2O nanoparticles after reduction with L—ascorbic acid, which confirms the absence of the core–shell structure, as explained above.

Figure 3a shows the SEM image of Cu/Cu_2O nanocomposite. We see that the composite has a cubic structure. In order to confirm that the powder is the nanocomposite, not the mixture of Cu and Cu_2O particles, the high—resolution TEM technique is used and the image is shown in Figure 3b, which demonstrates the direct reduction in the Cu_2O surface layer to form Cu dots to form the nanocomposite. Figure 3b also shows the (1 1 1) orientation of the crystals of both Cu and Cu_2O. The measured d spacing is 0.115 nm and 0.261 nm for Cu and Cu_2O, respectively, which is approximately the same as calculated from Bragg's Law (Table 1).

The powder nanocomposite of the ST sample was analyzed by powder X-ray diffraction. The XRD pattern was shown in Figure 4a. It shows that the peaks of Cu_2O at $2\theta = 29.51°$, 36.37°, 42.26°, 61.36°, 73.664°, and 77.38° correspond to planes (1 1 0), (1 1 1), (2 0 0), (2 2 0), (3 1 1), and (2 2 2), respectively, and matched well with ICDD #01—078—2076 [16]. In addition to the peaks of Cu_2O, the peaks of Cu also appeared at $2\theta = 43.27°$, 50.41°, and 74.14°; correspond to planes (1 1 1), (2 0 0), and (2 2 0), respectively; matched well with ICDD #785—1326 [17]. This indicates that the Cu/Cu_2O nanocomposite was successfully synthesized at ambient temperature using a simple aqueous chemical solution approach. To confirm the compounds of powder samples, the RIR is very useful for elucidating the composition of sample. Figure 4b was obtained by fitting the diffraction pattern using the Match! software. It is evident that the ST sample only contains two compounds (Cu_2O and Cu). Here, Cu_2O accounts for 60.1%, and the rest is Cu (39.1%). No by—product (such as CuO) or residual product ($Cu(OH)_2$) remains in the sample after the completion of the synthesis. Moreover, the Rietveld refinement method was used to compare with the XRD database of the ST sample. It used MAUD software to scan the standard spectra of Cu_2O (Pn—3 m, COD 1000063) and Cu (Fm—3 m, COD 5000216) based on the ST's XRD database. Some scanning criteria that were used include crystal structure, strain, quantitation, and texture in this method. The scanning results of Cu_2O and Cu were shown in Figure 4c,d, respectively. It is clear that the peaks at 29.51°, 36.37°, 42.26°, 61.36°, 73.664°, and 77.38° matched well with COD 1000063 of Cu_2O, and the remaining peaks at 43.27°, 50.41°, and 74.14° agreed with COD 5000216 of Cu. Hence, good scanning refinement was achieved for both Cu and Cu_2O. From the above discussion, we can conclude that the sample is nanocomposite and not a mixture of Cu and Cu_2O particles.

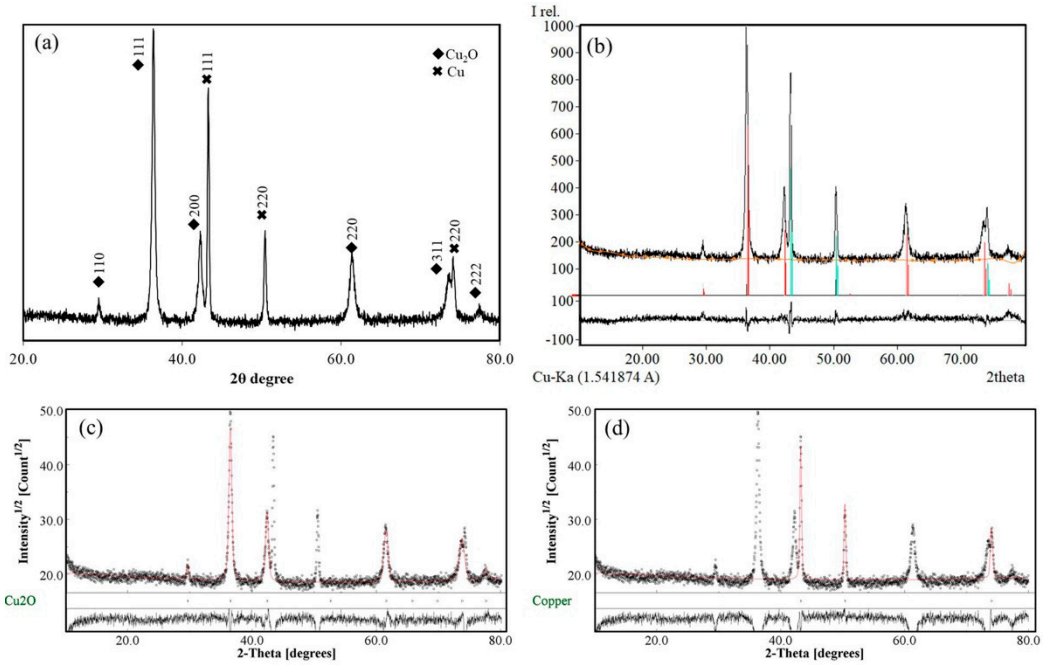

Figure 4. (**a**) XRD pattern of ST nanocomposite. (**b**) The XRD fitting pattern uses the reference intensity ratio (RIR) method. Note: the black spectrum is the XRD pattern of the ST sample; the red lines are the standard peak positions of Cu_2O (Ref: 96-101-0942); the green lines are the standard peak positions of Cu (Ref: 96-901-3015); orange line is background, and the spectrum below the *x*-axis is the different histogram obtained after fitting; and the Rietveld refinement is based on the XRD database with (**c**) Cu_2O and (**d**) Cu standard spectra. Note: The dots in subfigures (**c**) and (**d**) represent the standard peaks of Cu_2O and Cu, respectively. The green line and red line represent the XRD peaks of Cu_2O and Cu when fitted with the standard peaks in COD, respectively. The under spectrum ranges show the match of the XRD peak with the peaks in COD, whereas the wider the peaks here show the mismatch of the XRD peak with the COD peak.

3.2. The XRD Analysis of Cu/Cu_2O Powder Nanocomposites

In order to investigate the lattice parameter and crystalline size of NPs under the changing conditions in the reduction phase, the powder XRD technique was used to analyze all the samples, as shown in Figure 5a,b. From these diffraction patterns, the detectable peaks were similar to the obtained peaks from the ST sample, including six peaks of Cu_2O (ICDD #01—078—2076) and three peaks of Cu (ICDD #785—1326). The intensity versus 2θ plotted the difference under T_v and S_v. Normally, the crystalline size was calculated by the Scherrer equation with the XRD database (Equation (2)) [18]. The dislocation of crystal which is one of the lattice parameters considered by lattice strain and calculated by Williamson–Smallman's equation (Equation (3)) [17]:

$$D = \frac{K \cdot \lambda}{\beta \cdot \cos\theta} \quad (2)$$

$$\delta = \frac{1}{D^2} \quad (3)$$

$$\varepsilon = \frac{\beta \cdot \cos\theta}{4} \quad (4)$$

where D, K, λ, β, θ, and δ are the average crystallite size (nm), Scherrer constant, X-ray wavelength, FWHM, the Bragg's angle in degrees, and dislocation of crystal, respectively. Additionally, the lattice strain (ε) was calculated by Equation (4) [19,20]. The results are given in Table 2. The increases in T_v and S_v led to the increase in movement of all the ions,

molecules, and particles in all processes and led to the shifting and widening of Bragg's peaks in the XRD patterns. Thus, the crystallite size values calculated using the Scherrer equation were decreased due to the increase in the dislocation, the lattice strain, and the FWHM [21,22]. Furthermore, the inter—planar spacing values of all samples are of similar lengths, reflecting similar Bragg's peak positions.

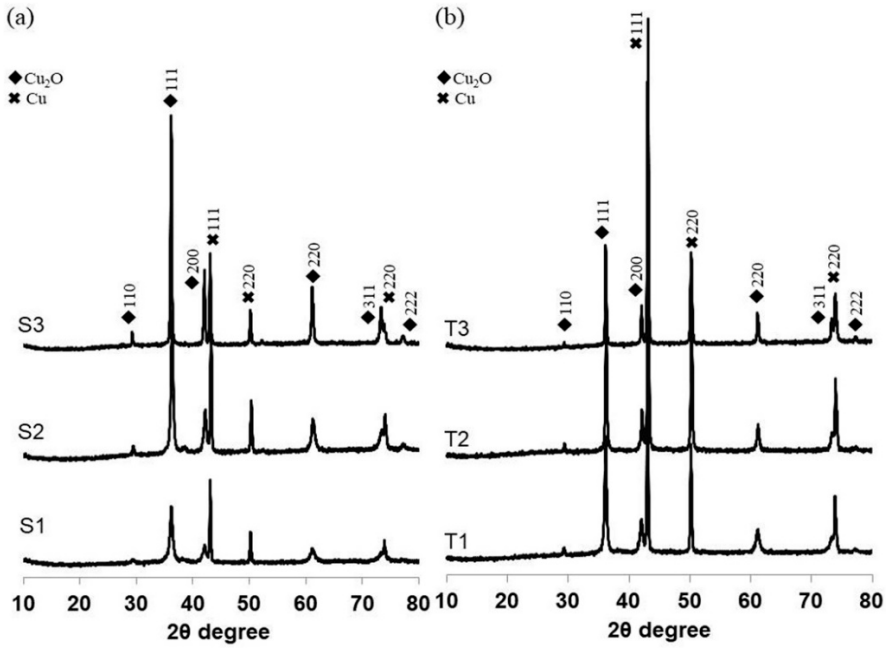

Figure 5. XRD patterns of nanocomposites in different (**a**) stirring speed and (**b**) reaction temperature.

Table 2. The important crystal parameters are calculated from XRD patterns of nanocomposites.

Title 1		ST	S1	S2	S3	T1	T2	T3
Crystallographic Parameters (from ICDD)	Crystal system	Cubic	Cubic	Cubic	Cubic	Cubic	Cubic	Cubic
	Space group	Pn—3 m	Pn—3 m	Pn—3 m	Pn—3 m	Pn—3 m	Pn—3 m	Pn—3 m
	a = b = c	4.260	4.258	4.258	4.258	4.267	4.267	4.258
	α = β = γ	90	90	90	90	90	90	90
	Volume of cell (nm^3)	0.0773	0.0772	0.0772	0.0772	0.0777	0.0777	0.0772
Inter—planar spacing (Å)		1.8703	1.9517	1.8727	1.8803	1.9537	1.8765	1.8800
Lattice parameter [Å]		4.0531	4.1206	4.0586	4.0730	4.0466	4.0657	4.0728
Full width at half maximum		0.3218	0.3273	0.3367	0.3554	0.3341	0.3354	0.3530
Dislocation—δ (nm)		0.0877	0.0894	0.0960	0.1069	0.0932	0.0952	0.1054
Lattice strain (%)		0.0708	0.0729	0.0741	0.0783	0.0744	0.0739	0.0778
Crystallite size (nm)		3.3881	3.3547	3.2389	3.0694	3.2862	3.2516	3.0906
Nelson Riley	Precise lattice parameter	3.9324	4.1089	3.9388	3.9373	3.9386	3.9377	3.9400
Williamson-Hall	Induced—lattice strain (%)	0.0623	0.1358	0.2280	0.1949	0.1832	0.1915	0.1461
	Induced—crystallite size (nm)	0.2512	0.1454	0.0591	−0.0189	0.0152	0.0106	−0.0098

As many previous reports have shown, in the wet chemical synthesis method, the nucleation phase is supported by high temperatures, while the growth phase is supported by low temperatures [23,24]. This means that the nanoparticles tend to be larger at lower temperatures, and an increase in temperature during the reaction leads to an increase in size. Furthermore, the decrease in particle size with raising the temperature in the synthesis process is generally considered to increase the reaction rate under higher temperatures [23,25]. Furthermore, increasing the T_v leads to thermal expansion of the nanoparticle's unit cell, thereby increasing the lattice constant [26]. Specifically, the lattice parameter increased

from 4.0513 Å to 4.0539 Å, 4.0657 Å, and 4.0728 Å, corresponding to 40 °C, 60 °C, 80 °C, and 100 °C, respectively.

Stirring speed plays an important role in nanoparticle synthesis, creating the homogeneous distribution of all compounds and giving all compounds more opportunity to react and bind together. However, several reports showed that increasing S_v can decrease the particle size [27,28]. Consistent with these results, we observed in the microstructure analysis (Table 2) that the crystallite size of the samples decreased with increasing S_v. Particularly, the increased stirring speed from 50 to 550 rpm reduced the size of the nanocomposites from 3.3881 to 3.0694 nm. However, the lattice parameter and inter—planar spacing did not follow this downtrend. Further increasing the stirring speed, the size of these nanocomposites decreased significantly along with a random size distribution of the inter—planar and lattice parameter [27]. Furthermore, particles formed under the intense stirring speeds would have a higher chance to collide with other particles during the aging stage. As a result, the edges, corners, and surface of the particles will be abraded, and hence, the crystalline size will also be reduced.

To gain insight into the changes in NPs under extreme conditions during synthesis, some methods and fitting models were employed in the analysis. We investigated how increases in the width and the intensity, and how shifting the positions of the peaks were affected by the crystallite size and lattice strain using the Williamson-Hall (W-H) method. This method is an effective method for calculating the induced—lattice strain and induced—crystallite size because it uses breadth integration [18]. This method reduces strain—induced voltage and size expansion by treating the peaks of the XRD pattern as a function of 2θ. The lattice strain and crystal size were obtained from the linear regression equation between 2sinθ and βcosθ. The y—intercept was used to estimate the crystallite size, and the slope was used to fit the lattice strain. Table 2 and Figure 6 show the matching results of the XRD database with the W-H model. From these results, the increases in T_v and S_v led to a decrease in the induced—crystallite size. The induced—crystallite size values calculated using the W-H method were smaller than the calculated values from the Scherrer equation. Moreover, the negative y—intercept values of S3 and T3 (−0.0189 and −0.0098, respectively) indicated the shriveling of crystals [9].

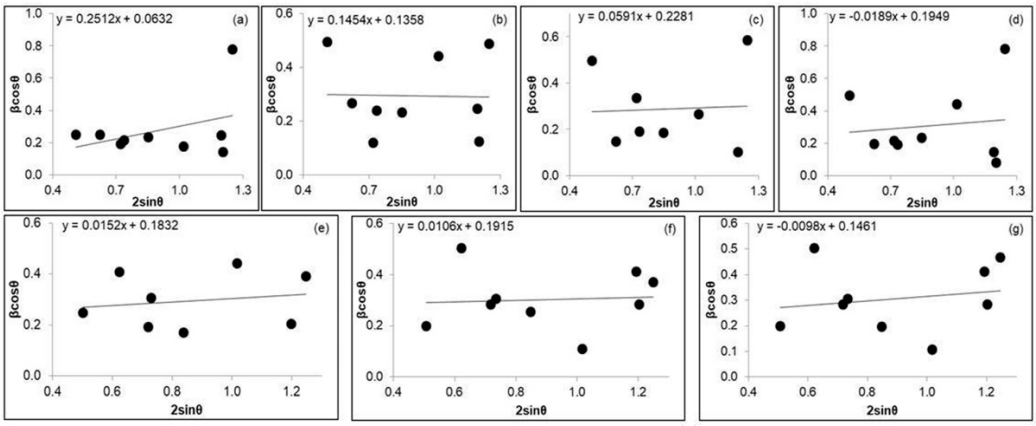

Figure 6. The linear regression between 2*sinθ* and *βcosθ* of W-H method with (**a**) ST, (**b**) S1, (**c**) S2, (**d**) S3, (**e**) T1, (**f**) T2, and (**g**) T3.

Due to the influence of T_v and S_v, the crystal growth in all experiments is not perfect, so the lattice parameter is different from the ICDD (4.2696 Å). Therefore, the Nelson-Riley function (Equation (5)) [17] was used to recalculate the precise lattice parameter (PLP) from the XRD database.

$$f(\theta) = \frac{\frac{\cos^2\theta}{\sin\theta} + \frac{\cos^2\theta}{\theta}}{2} \quad (5)$$

The PLP shown in Figure 7 and Table 2 was obtained from the linear regression relationship between the function f(θ) and the lattice parameter. The PLPs extracted have shorter values compared with the values obtained from ICDD library. To explain why the PLP values have shorter values, the process of measurement and calculation method should be considered. The lattice parameters are usually measured by the direct procedure. That means the d—spacing is calculated by Bragg's derivative (λ = 2dsinθ). In this measurement, the accuracy of the crystallographic parameter (a, b, c) and the d—spacing (d) depends entirely on the accuracy of the sin(θ) calculation [29]. Moreover, the Cu/Cu_2O nanocomposite in this research has a cubic structure ($a = b = c = d\sqrt{h^2 + k^2 + l^2}$) Therefore, $\Delta a = \Delta d\sqrt{h^2 + k^2 + l^2}$. Additionally, the term $\Delta a/a$ (or $\Delta d/d$) arises because of the error for the field in θ, which is the fractional error in a (or d). As θ approaches 90°, the fractional error approaches 0 [27]. Therefore, $\Delta a/a = \Delta d/a = -\cot\theta \cdot \Delta\theta$.

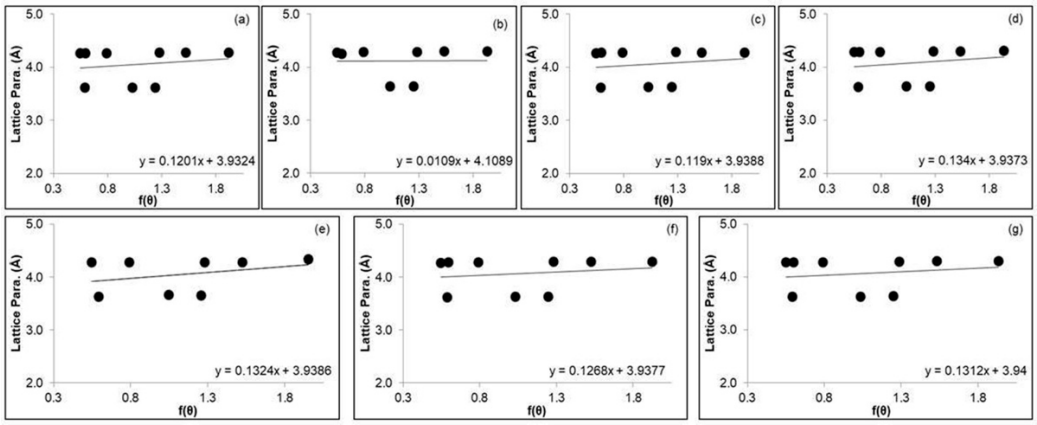

Figure 7. The linear regression between f(θ) function and lattice parameter of Nelson-Riley function with (**a**) ST, (**b**) S1, (**c**) S2, (**d**) S3, (**e**) T1, (**f**) T2, and (**g**) T3.

The key to achieving high accuracy in parametric measurements is the use of a back—reflected beam with a value of 2θ as close to 180° as possible [20,29]. When approaching 2θ = 180° (i.e., θ = 90°), the value of a will approach the true value. However, because measuring the value at 2θ = 180° will often be limited, it is necessary to plot the measured values, and then extrapolate to 2θ = 180° against some function of θ. Moreover, there are many systematic errors, such as the absorbance of the specimen; unintentional curvedness of the sample, affecting the diffraction angles; device error; etc. [30]. The linearity of the histogram at very high angles will provide an exact value of the lattice constant. Furthermore, this function is of great significance in determining the precise lattice constant because the error function becomes minimal when f(θ) = 90°, which corresponds to the anti—reverse reflection along the path of the incident beam [31]. Accordingly, using the Nelson-Riley function can reduce the systematic errors in the calculation process by using extrapolation from the peak positions to the magnitude 2θ.

Cu/Cu_2O nanocomposite has many potential applications. Understanding the changes in the crystallographic parameters under the changes of synthesized conditions, scientists can enhance the efficiency of materials. First, the adsorption capacity of nanoporous core–shell $Cu@Cu_2O$ nanocomposite in the methyl orange removal process was investigated [4], the particle size of samples was changed (300 nm to 4 μm) by changing the precursor concentration and reaction temperature, and the physic-sorption nature of methyl orange adsorption onto the $Cu@Cu_2O$ nanocomposite was revealed by the activation energy (Ea) of 12.4 kJ/mol in that research. Second, Chen [32] showed the potential of Cu/Cu_2O nanocomposite films in the solar cell, which can prevent the photo corrosion of the active layer and enhance the lifetime of perovskite solar cells. Furthermore, the combination of Cu/Cu_2O and Pd nanosheets in glucose sensors shows excellent electrochemical activity in the analysis of glucose in real blood samples [33].

4. Conclusions

In this study, Cu/Cu_2O nanocomposites were synthesized by the wet chemical method. The results of the XRD, SEM, and TEM analyses were used to confirm the composition and structure of nanocomposite. The compositions of the sample were also confirmed by the Rietveld refinement and RIR methods. Under a range of reaction times and stirring times, the crystallographic parameters changed. The Williamson-Hall method was helpful in determining that the induced—crystallite size was reduced with increasing T_v and S_v, and this size is also smaller than the result calculated by the Scherrer equation. Additionally, the Nelson-Riley function is used to recalculate the precise lattice parameters in less time than the results of Bragg's law. Furthermore, the control of reaction temperature and stirring speed can assist in controlling the crystal size of the nanocomposite through the reduction in lattice parameters (down from 4.12 to 4.07 Å) and inter—planar spacing (down from 1.95 to 1.88 Å).

Author Contributions: Writing—original draft preparation, Conceptualization, data interpretation, N.H.L. and N.T.N.T.; Data curation, Validation, Resource, Visualization, Formal analysis, N.L. and C.T.T.T.; Writing—review and editing, A.M.T., R.P.S. and M.S.T.; Data curation, Funding acquisition, S.A. and M.M.G.; Supervision, Project administration, J.H.J. All authors have read and agreed to the published version of the manuscript.

Funding: This research was funded by Researchers Supporting Program (TUMA-Project-2021-2), AlMaarefa University, Riyadh, Saudi Arabia.

Institutional Review Board Statement: Not applicable.

Informed Consent Statement: Not applicable.

Data Availability Statement: Not applicable.

Acknowledgments: The authors deeply acknowledge the Researchers Supporting Program (TUMA-Project-2021-2), AlMaarefa University, Riyadh, Saudi Arabia for supporting steps of this work.

Conflicts of Interest: The authors declare no conflict of interest.

References

1. Khiavi, N.D.; Katal, R.; Eshkalak, S.K.; Panah, S.M.; Ramakrishna, S.; Jiangyong, H. Visible light driven heterojunction photocatalyst of CuO–Cu_2O thin films for photocatalytic degradation of organic pollutants. *J. Nanomater.* **2019**, *9*, 1011. [CrossRef] [PubMed]
2. Gupta, D.; Meher, S.R.; Illyaskutty, N.; Alex, Z.C. Facile synthesis of Cu_2O and CuO nanoparticles and study of their structural, optical and electronic properties. *J. Alloys Compd.* **2018**, *743*, 737–745. [CrossRef]
3. Bayat, F.; Sheibani, S. Enhancement of photocatalytic activity of CuO—Cu_2O heterostructures through the controlled content of Cu_2O. *Mater. Res. Bull.* **2022**, *145*, 111561. [CrossRef]
4. Kou, T.; Wang, Y.; Zhang, C.; Sun, J.; Zhang, Z. Adsorption behavior of methyl orange onto nanoporous core–shell Cu@Cu_2O nanocomposite. *Chem. Eng. J.* **2013**, *223*, 76–83. [CrossRef]
5. Dai, J.; Fan, X.M.; Liu, H.; Wang, J.; Li, H.R.; Zhang, F.Z. Fabrication and high visible light photocatalytic properties of Cu/Cu_2O nanocomposites by the one—pot solution—phase hydrothermal method. *J. Nanosci. Nanotechnol.* **2012**, *12*, 6412–6419. [CrossRef]
6. Huan, K.; Tang, L.; Deng, D.; Wang, H.; Si, X.; Yan, X.; Luo, L. A Two-Step Electrodeposition of Pd—Cu/Cu_2O Nanocomposite on FTO Substrate for Non—Enzymatic Hydrogen Peroxide Sensor. *Curr. Anal. Chem.* **2021**, *17*, 1373–1381. [CrossRef]
7. Kamazani, M.M.; Zarghami, Z.; Rahmatolahzadeh, R.; Ramezani, M. Solvent-free synthesis of Cu-Cu_2O nanocomposites via green thermal decomposition route using novel precursor and investigation of its photocatalytic activity. *Adv. Powder Technol.* **2017**, *28*, 2078–2086. [CrossRef]
8. Nikam, A.; Bhagavatula, P.; Kulkarni, A. Wet Chemical Synthesis of Metal Oxide Nanoparticles: A Review. *CrystEngComm* **2018**, *20*, 5091–5107. [CrossRef]
9. Dey, P.C.; Sarkar, S.; Das, R. X-ray diffraction study of the elastic properties of jagged spherical CdS nanocrystals. *Mater. Sci.-Pol.* **2020**, *38*, 271–278. [CrossRef]
10. Mote, V.; Purushotham, Y.; Dole, B. Williamson–Hall analysis in estimation of lattice strain in nanometer-sized ZnO particles. *J. Theor. Appl. Phys.* **2012**, *6*, 6. [CrossRef]
11. Uvarov, V.; Popov, I.; Shapur, N.; Abdin, T.; Gofrit, O.N.; Pode, D.; Duvdevani, M. X-ray diffraction and SEM study of kidney stones in Israel: Quantitative analysis, crystallite size determination, and statistical characterization. Environ. *Geochem. Health* **2011**, *33*, 613–622. [CrossRef] [PubMed]

12. Phan, C.M.; Nguyen, H.M. Role of capping agent in wet synthesis of nanoparticles. *J. Phys. Chem. A* **2017**, *121*, 3213–3219. [CrossRef] [PubMed]
13. Thanh, N.T.; Maclean, N.; Mahiddine, S. Mechanisms of nucleation and growth of nanoparticles in solution. *Chem. Rev.* **2014**, *114*, 7610–7630.
14. Elechiguerra, J.L.; Lopez, L.L.; Liu, C.; Gutierrez, D.G.; Bragado, A.C.; Yacaman, M.J. Corrosion at the nanoscale: The case of silver nanowires and nanoparticles. *Chem. Mater.* **2005**, *17*, 6042–6052. [CrossRef]
15. Jasbi, N.E.; Dorranian, D. Effect of aging on the properties of TiO_2 nanoparticle. *J. Theor. Appl. Phys.* **2016**, *10*, 157–161. [CrossRef]
16. Collins, D.; Luxton, T.; Kumar, N.; Shah, S.; Walker, V.K.; Shah, V. Assessing the Impact of Copper and Zinc Oxide Nanoparticles on Soil: A Field Study. *PLoS ONE* **2012**, *7*, e42663. [CrossRef]
17. Lam, N.H.; Le, N.; Kim, E.S.; Tamboli, M.S.; Tamboli, A.M.; Truong, N.T.N.; Jung, J.H. Powder X-ray diffraction analysis of Cu/Cu_2O nanocomposites synthesized by colloidal solution method. *Korean J. Chem. Eng.* 2022. [CrossRef]
18. Mishra, S.K.; Roy, H.; Lohar, A.K.; Samanta, S.K.; Tiwari, S.; Dutta, K. A comparative assessment of crystallite size and lattice strain in differently cast A356 aluminium alloy. *IOP Conf. Ser. Mater. Sci. Eng.* **2015**, *75*, 012001. [CrossRef]
19. Hameed, T.A.; Wassel, A.R.; IRadaf, M.E. Investigating the effect of thickness on the structural, morphological, optical and electrical properties of $AgBiSe_2$ thin films. *J. Alloys Compd.* **2019**, *805*, 1–11. [CrossRef]
20. Ansari, A.R.; Hammad, A.H.; Abdel-wahab, M.S.; Shariq, M.; Imran, M. Structural, optical and photoluminescence investigations of nanocrystalline CuO thin films at different microwave powers. *Opt. Quantum Electron.* **2020**, *52*, 426–441. [CrossRef]
21. Fayaz, A.M.; Balaji, K.; Kalaichelvan, P.T.; Venkatesan, R. Fungal based synthesis of silver nanoparticles—an effect of temperature on the size of particles. *Colloids Surf. B* **2009**, *74*, 123–126. [CrossRef] [PubMed]
22. Zhang, J.Y.; Shen, Z.G.; Zhong, J.; Hu, T.T.; Chen, J.F.; Ma, Z.Q.; Yun, J. Preparation of amorphous cefuroxime axetil nanoparticles by controlled nanoprecipitation method without surfactants. *Int. J. Pharm.* **2006**, *323*, 153–160. [CrossRef] [PubMed]
23. Liu, H.; Zhang, H.; Wang, J.; Wei, J. Effect of temperature on the size of biosynthesized silver nanoparticle: Deep insight into microscopic kinetics analysis. *Arab. J. Chem.* **2017**, *13*, 1011–1019. [CrossRef]
24. Jiang, X.C.; Chen, W.M.; Chen, C.Y.; Xiong, S.X.; Yu, A.B. Role of Temperature in the Growth of Silver Nanoparticles Through a Synergetic Reduction Approach. *Nanoscale Res. Lett.* **2010**, *6*, 32. [CrossRef]
25. Kasture, M.B.; Patel, P.; Prabhune, A.A.; Ramana, C.V.; Kulkarni, A.A.; Prasad, B.L.V. Synthesis of silver nanoparticles by sophorolipids: Effect of temperature and sophorolipid structure on the size of particles. *J. Chem. Sci.* **2008**, *120*, 515–520. [CrossRef]
26. Albetran, H.M. Thermal expansion coefficient determination of pure, doped, and co-doped anatase nanoparticles heated in sealed quartz capillaries using in—situ high—temperature synchrotron radiation diffraction. *Heliyon* **2020**, *6*, e04501. [CrossRef]
27. Aravand, M.A.; Semsarzadeh, M.A. Particle Formation by Emulsion Inversion Method: Effect of the Stirring Speed on Inversion and Formation of Spherical Particles. *Macromol. Symp.* **2008**, *274*, 141–147. [CrossRef]
28. Lemos, Y.P.; Marfil, P.H.M.; Nicoletti, V.R. Particle size characteristics of buriti oil microcapsules produced by gelatin—sodium alginate complex coacervation: Effect of stirring speed. *Int. J. Food Prop.* **2017**, *20*, 1438–1447. [CrossRef]
29. Suryanarayana, C.; Norton, M.G. *X-ray Diffraction a Practical Approach*, 1st ed.; Plenum Press: New York, NY, USA, 1998; p. 513.
30. Cullity, B.D.; Stock, S.R. *Elements of X-ray Diffraction*, 3rd ed.; Prentice-Hall: New York, NY, USA, 2001; pp. 363–383.
31. Das, R.; Sarkar, S. Determination of structural elements of synthesized silver nano—hexagon from X-ray diffraction analysis. *Indian J. Pure Appl. Phys.* **2018**, *56*, 765–772.
32. Chen, Y.J.; Li, M.H.; Huang, J.C.A.; Chen, P. Cu/Cu_2O nanocomposite films as a p-type modified layer for efficient perovskite solar cells. *Sci. Rep.* **2018**, *8*, 7464. [CrossRef]
33. Tang, L.; Huan, K.; Deng, D.; Han, L.; Zeng, Z.; Luo, L. Glucose sensor based on Pd nanosheets deposited on Cu/Cu_2O nanocomposites by galvanic replacement. *Colloids Surf.* **2020**, *188*, 110797. [CrossRef] [PubMed]